Prediction of Radiation Belts Electron Fluxes at a Low Earth Orbit Using Neural Networks With PROBA-V/EPT Data

Edith Botek[1] [ID], **Viviane Pierrard[1,2]** [ID], and **Alexandre Winant[1]** [ID]

[1]Space Physics and Solar Terrestrial Center of Excellence (STCE), Royal Belgian Institute for Space Aeronomy, Brussels, Belgium, [2]Center for Space Radiations, ELIC, Université Catholique de Louvain, Louvain-La-Neuve, Belgium

Abstract We introduce for the first time the PROBA-V/EPT electron flux data to train a deep learning data-driven model with the purpose of investigating the Earth's radiation belts dynamics. The Long-Short Term Memory Neural Network is employed to predict the electron fluxes between 1 and 8 Earth Radius (R_E) along a Low Earth Orbit. Different combinations of time series inputs involving Solar Wind and geomagnetic data are tested, based on previous knowledge of their impact onto the high energy radiation fluxes. Two Energetic Particle Telescope energy channels feed the learning procedure for nonrelativistic (0.5–0.6 MeV) and relativistic (1.0–2.4 MeV) electron fluxes. A good performance of the model employing different time resolutions from hours to days is demonstrated with a correlation of more than 0.9 between the predicted and out-of-sample fluxes, and a prediction efficiency that can attain between 0.6 and 0.9 depending on the L range. The analysis of different input parameters and time resolutions allows to construct the best data set structure and improve the model to identify relevant effects such as dropouts, flux increase and recovery features.

Plain Language Summary The Van Allen belts are regions of intense radiation trapped by the Earth's magnetic field. A continuous stream of charged particles, the solar wind, is ejected from the Sun's outer atmosphere carrying the interplanetary magnetic field. When the solar wind interacts with the Earth's magnetic field, it can have significant effects on the space environment surrounding our planet. Predicting the state of the Van Allen Belts is crucial for satellites orbiting near-Earth, and to aviation and astronaut operations. Disturbances in the Van Allen Belts can represent a significant hazard to human activities, and can also drive out-of-control induced electric currents that can damage equipment on satellites. A Machine Learning model is developed here using electron radiation fluxes measurements from an instrument called Energetic Particle Telescope, onboard the PROBA-V satellite orbiting at an altitude of 820 km. A good performance of the model is demonstrated with a prediction efficiency between 0.6 and 0.9. The results of the model support the prediction of the space-time Van Allen belts evolution to prevent serious damage in case of strong external perturbations from particles and electromagnetic fields.

1. Introduction

The Van Allen radiation belts constitute a zone with high-energy charged particles trapped in the magnetic field surrounding the Earth. Such a population of particles interacts in complex ways with lower energy particles (ionosphere, plasmasphere, and plasmatrough), and with electromagnetic waves of different frequencies (Baker, 2021; Koskinen & Kilpua, 2022). The more energetic particles are accelerated by diverse mechanisms involving plasma particles and waves (see e.g., Li & Hudson, 2019; Reeves et al., 2003; Thorne et al., 2013). The Van Allen radiation belts consist of two main regions: the inner and outer belts. The inner belt is more stable and primarily composed of protons. The outer belt, on the other hand, is filled mainly with electrons, highly influenced by external sources such as solar wind (Turner et al., 2019). Between the inner and outer belts, there exists a slot region that contains very low particle fluxes. During active solar conditions, significant particle fluxes migrate from the outer belt to the slot region following the effects of the magnetopause shadowing, and they can even attain the inner belt (Reeves et al., 2016). This overpopulation decays in several hours to days depending on the energy of the particles, and if the space weather conditions lie down to normal. The population of energetic electrons of the radiation belts ranges from a few keV to tens of MeV, playing a threatening role in near-Earth spacecraft operations. The thousands of satellites orbiting the Earth for monitoring, communications, and other scientific purposes are constantly exposed to perturbations due to charged electrons of low energy contributing to surface charging anomalies and to more energetic particles that engender deep charging to the satellite devices (Garrett, 2016). Both phenomena can be mitigated with a better knowledge and forecast of the
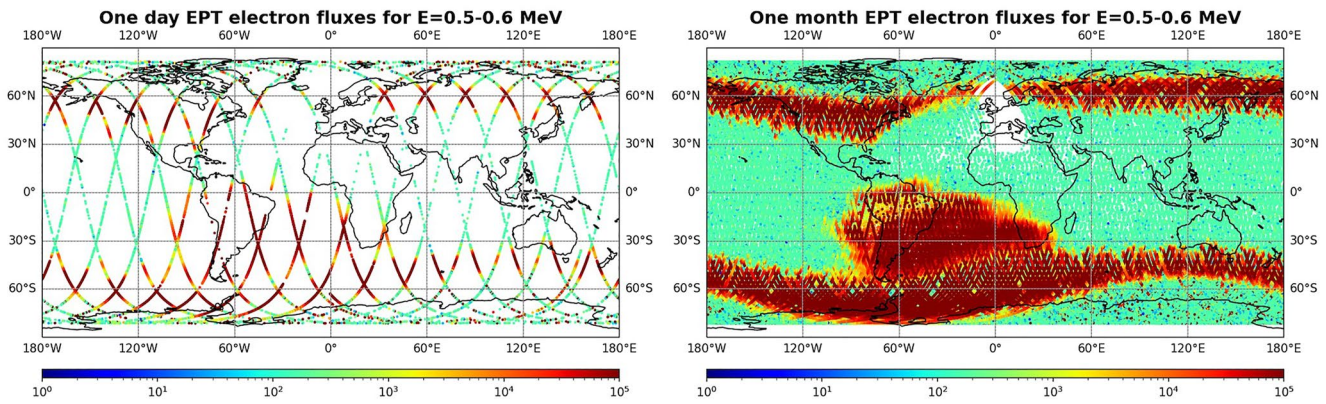
Figure 1. PROBA-V/EPT coverage displaying the 0.5–0.6 MeV electron fluxes in #/(cm² s sr MeV) along the orbit during June 23 (left) and the entire month of June (right) in 2015.

radiation environment dynamics. This is a very difficult task that can be hardly overcome nowadays by smartly using available measured data combined to physical knowledge.

Many works have arisen these last two decades where the satellite measurements in the inner magnetosphere have been used to figure out radiation belt dynamics and, more recently, to train machine learning models. The Geostationary Operational Environmental Satellite network with its fleet of geosynchronous equatorial orbit (GEO) satellites launched since the seventies (https://www.nasa.gov/content/goes) have been extensively employed for such goal (see e.g., Landis et al., 2022; Myagkova et al., 2019; Son et al., 2022; Sun et al., 2021; Wei et al., 2018). The launch of Radiation Belt Storm Probes (RBSP) in 2012 in a Low-Medium Earth orbit with a highly elliptic equatorial trajectory (Mauk et al., 2012), later renamed Van Allen Probes, has enormously contributed to the research on the physical processes governing the radiation belts and revamped our knowledge of the near-Earth space by demonstrating, for example, the existence of a third ultra-relativistic radiation belt (Mann et al., 2016) during high geomagnetic activity. Hence, data from RBSP are being used routinely, even after their decommissioning in 2019, as driven parameters for machine learning models (see e.g., Chu et al., 2021; Ma, Bortnik, et al., 2022; Ma, Chu, et al., 2022; Wing, Turner, et al., 2022) and also combined with other satellite data as from Los Alamos National Laboratory GEO satellite and NOAA Low Earth Orbit (LEO) Polar Operational Environmental Satellite (POES) (de Lima et al., 2020) to feed the PreMev model. Other LEO satellite data driving such kind of works come from the Global Positioning System (Smirnov et al., 2020) for the MERLIN model or the POES data for the SHELLS model (Claudepierre & O'Brien, 2020). This list of examples is not exhaustive.

In the present work, the PROBA-V/EPT high-energy electron data are prototypically employed to train a deep-learning model. The next section illustrates the EPT measurement features and mentions previous works using the data. The OMNIWEB solar wind and geomagnetic data retrieved as input for the model are also introduced. Section 3 describes the NN model developed for the forecast of electron fluxes time series in LEO, and the group of parameters selected to test the model. Section 4 gathers the results, and the final conclusions are elaborated in Section 5 together with an outlook of future developments.

2. Data

2.1. PROBA-V/EPT Data

The Energetic Particle Telescope (EPT) was launched in May 2013 onboard PROBA-V satellite (Cyamukungu et al., 2014) on a LEO of 98.7° inclination at 820 km of altitude and with a 101.21 min period. The average pitch angle varies between 60° and 120°. The EPT discriminates between electrons, protons and helium ions in energy ranges 0.5–20 MeV, 9.5–300 MeV and 38–1,200 MeV, distributed in 6, 10, and 10 channels, respectively, with a time resolution of 2 s. Figure 1 illustrates the instrument measurements during a day of satellite world coverage (left) and a month (right) path. Missing data over Europe correspond to the 10:30–11:30 Local Time at Descending Node (Pierrard et al., 2014). The processed data are available at https://swe.ssa.esa.int/space-radiation.
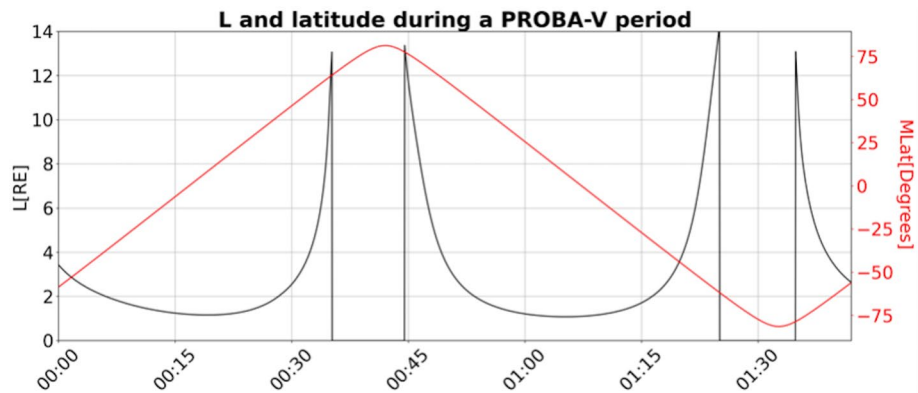
Figure 2. L-shell parameter (black) and magnetic latitude variation (red) during a PROBA-V orbit in 15 June 2015.

Because of its polar orbit, the satellite presents a very quick variation in L-shells (McIlwain, 1961) along its trajectory, especially close to the poles, as it can be noticed in Figure 2 where a whole orbit period is represented in L (left) and geomagnetic latitude (right) axis. After about 30 min of orbit along low L-shells (twice during the period), the spacecraft sweeps nearly all the L-shells in about 10 min from one pole to the other about four times in a period. The instrument operation for 9 years now allows the investigation of many aspects of the Van Allen radiation belts. Indeed, the EPT electron fluxes have been analyzed to a wide extent along several works (Cunningham et al., 2020; Pierrard et al., 2019, 2020, 2021, 2022), also correlating the data with other spacecraft and confirming different mechanisms of particles sources and losses. Figure 3 displays electron fluxes from 2015 to 2018 for two EPT channels (top and middle panels) covering non-relativistic ($E = 0.5$–0.6 MeV) and relativistic ($E = 1.0$–2.4 MeV) energies. Geomagnetic activity, represented in the figure by the Disturbance
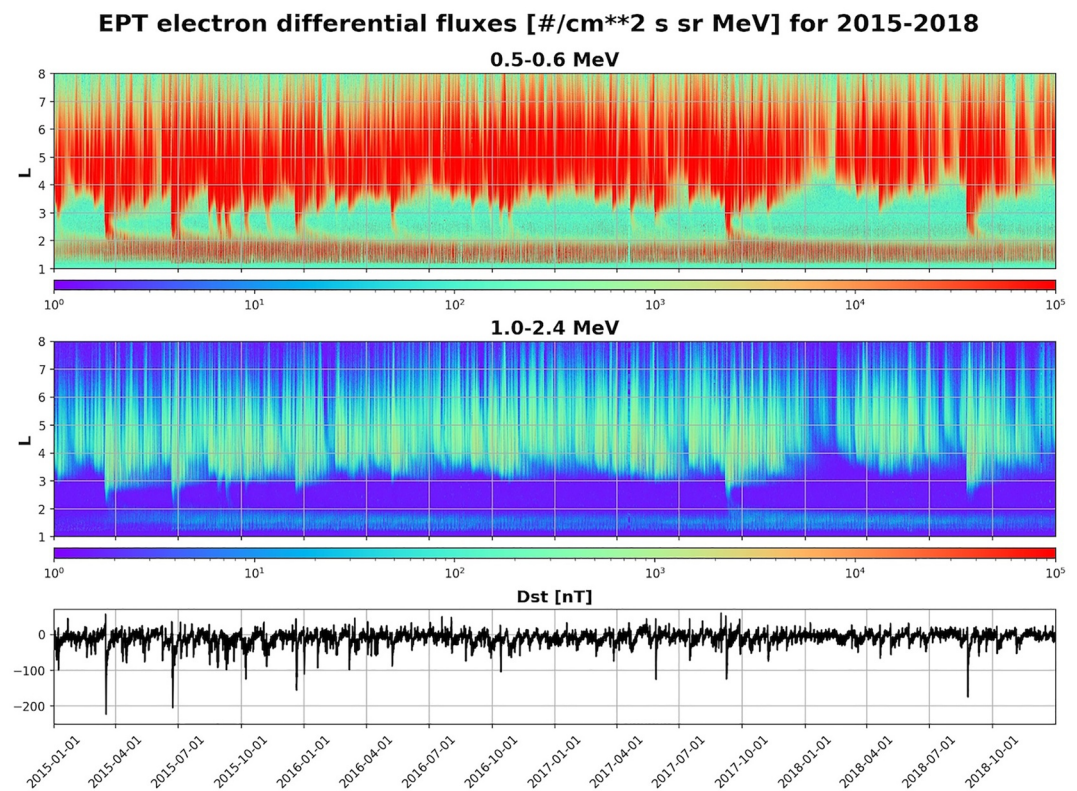

Figure 3. PROBA-V/EPT electron fluxes at $L = 1$–8 R_E for two energy channels: 0.5–0.6 MeV (top panel), 1.0–2.4 MeV (middle panel) together with Dst data (bottom panel) during 2015–2018.
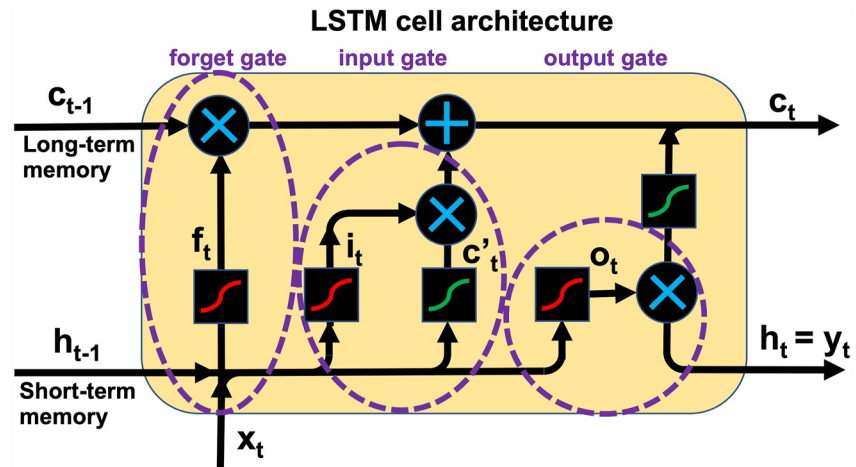
Figure 4. Long-Short Term Memory time-step cell structure.

storm time (Dst) index (bottom panel), has severely perturbed the electron fluxes on many occasions during the selected period generating dropouts, flux enhancements, injections to the slot region and some of them to the inner belts, as well as long flux relaxation times. The strongest geomagnetic storms provoked deep injections of lower energy fluxes until the inner belt, several times during 2015, once in 2017 and once in 2018, whereas fewer fluxes of higher energy penetrate down under the slot. The present work will focus on predicting the fluxes variations for these particular energy channels, which we will denote e1 and e5, respectively, all along the article. More precisely, the logarithm with base 10 of the corresponding fluxes, named Log(e1) and Log(e5), will be the predicted quantities. The time series of logarithmic electron fluxes as well as the satellite coordinates L, Magnetic Local Time (MLT) and Latitude (denoting the geomagnetic latitude) resampled, in a first stage, at 1-min resolution have been selected as input data.

2.2. OMNI Data

Given the numerous works that have already systematically analyzed the solar wind and geomagnetic parameters that better drive the machine learning procedure for the radiation belts (see references cited in the introduction section), we have restricted the time series to the following data. As for geomagnetic indices, the SYMmetric disturbances parallel to the Earth magnetic dipole (SYM/H index), which is essentially similar to the Dst index (1-hr resolution) but with a higher time resolution (1-min) (Wanliss & Showalter, 2006), was selected together with the Auroral electrojet Lower index (AL) (Weygand et al., 2014). Regarding the Solar Wind parameters, we kept only the Solar Wind speed (SWSpeed) and pressure (SWPressure). The geomagnetic and solar wind data sets at 1-min resolution have been extracted from the (https://omniweb.gsfc.nasa.gov/).

3. Method

3.1. Neural Network Model

The Long-Short Term Memory (LSTM) deep learning method was selected for this work (Hochreiter & Schmidhuber, 1997) by using the Keras library in the framework of the Tensorflow platform (Abadi et al., 2016). LSTM is an advanced Recurrent Neural Network capable of remembering long-term dependencies into the learning procedure (Géron, 2022). The basic architecture of LSTM (see Figure 4) is a cell where the information flow at each time step "t" traverses three gate controllers with the purpose of forgetting the useless memories, including the current inputs and providing new outputs for the next cell or as final results. The forget gate combines long-term and short-term memories coming from the previous cell step c_{t-1} and h_{t-1}, respectively, where "c" states for cell and "h" states for "hidden." The input gate incorporates to the current time step new inputs (x) that influence the candidate cell state (c') and the output gate elaborates the cell results (y).

The corresponding equations have the following form:

$$i_t = \sigma(W_{xi} \times x_t + W_{hi} \times h_{t-1} + b_i) \tag{1}$$

$$f_t = \sigma(W_{xf} \times x_t + W_{hf} \times h_{t-1} + b_f) \tag{2}$$

$$o_t = \sigma(W_{xo} \times x_t + W_{ho} \times h_{t-1} + b_o) \tag{3}$$

$$c'_t = tanh(W_{xc'} \times x_t + W_{hc'} \times h_{t-1} + b_{c'}) \tag{4}$$

$$c_t = f_{t'} \bigotimes c_{t-1} \bigoplus i_t \bigotimes c'_t \tag{5}$$

$$y_t = h_t = o_t \bigotimes tanh(c_t) \tag{6}$$

where W_x and W_h are the weight matrices for the connection to the inputs x_t and to a previous short-term state h_{t-1}, respectively, that feed the four layers of the cell: forget (f), input (i), output (o) and the candidate cell state (c'). The biases "b" provide a particular contribution to each of the layers in order to better adjust the outputs. The three first layers are activated by a Sigmoid function:

$$\sigma(z) = \frac{1}{1 + e^{-z}} \tag{7}$$

and the candidate cell state by a Tangent Hyperbolic function:

$$tanh(z) = \frac{e^z - e^{-z}}{e^z + e^{-z}} \tag{8}$$

The time series of EPT logarithmic electron fluxes spanning 2015–2018 data together with the PROBA-V satellite coordinates, solar wind and geomagnetic data for the same time period were merged and interpolated when necessary. Next, the time series data set containing all the variables has been resampled to 1-hr and to 1-day resolution for the training and predicting instances as discussed later in Section 4. The whole data set was then split as follows: 60% was assigned to the "train" series and 30% was allocated to "validation" to monitor the accuracy of the training while tuning the model hyperparameters. The remaining 10% was kept as the "test" data set, which is employed later for testing the prediction effectiveness of the model. Then, the whole period of 4 years was split like this: train = 1 Jan 2015–15 July 2017; validation = 15 July 2017–5 August 2018; test = 5 August 2018–31 December 2018.

3.2. Model Hyperparameters

The whole data set was preprocessed using the StandardScaler tool (https://scikit-learn.org/stable/modules/preprocessing.html), which is a common re-scaling procedure in machine learning to standardize the data containing many outliers and with very different variable ranges. The inverse transformation is applied to the outputs at the end of the predicting procedure to recover the real values ranges. The NN model was trained with two LSTM layers containing 64 and 8 units. The Mean Square Error (MSE) was used as loss for the compilation step with the Adam optimizer to improve the model. Two parameters were activated for the fitting procedure: (a) the "Early Stopping" parameter to stop training when the monitoring metrics (the loss given by the validation data set) is no longer improving; and (b) the "Model Checkpoint" (together with the setting save_best_only = True according to the monitored loss) to save the best model state. This best saved state can be loaded afterward to directly make predictions.

3.3. Input Features

Following the work already performed in many previous articles (see e.g., Landis et al., 2022; Ma, Bortnik, et al., 2022; Ma, Chu, et al., 2022; Smirnov et al., 2020; Wei et al., 2018; Wing, Johnson, et al., 2022; Wing, Turner, et al., 2022, and references cited therein) for the selection of the input variables to predict electron fluxes in the radiation belts, we have pre-selected the parameters displayed on the heatmap correlation of Figure 5. The correlations were evaluated here with the whole data set spanning 2015–2018. Only the case of e1 channel
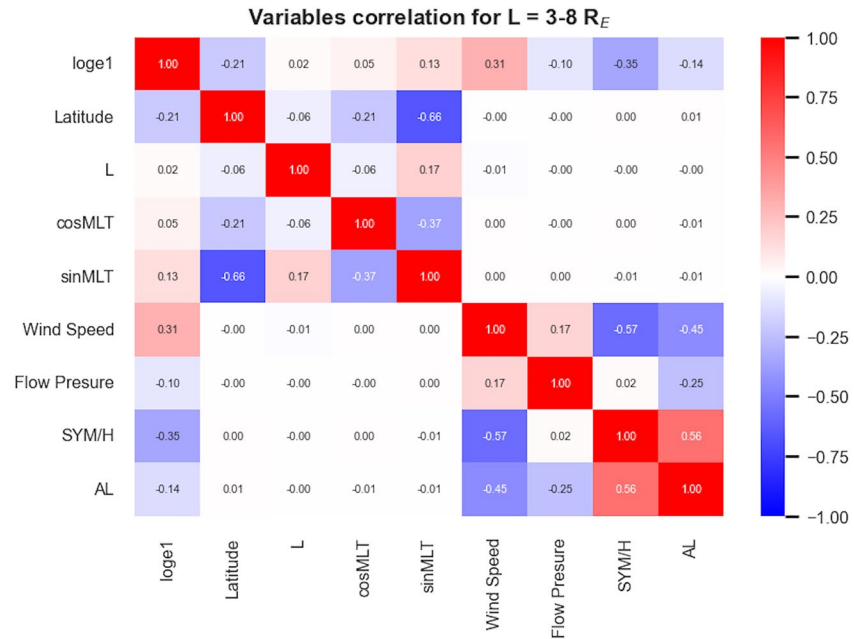
Figure 5. Correlation matrix between PROBA-V/EPT logarithmic electron fluxes, satellite coordinates, solar wind and geomagnetic parameters.

for $L = 3–8$ R_E is displayed and discussed here since the conclusions remain identical for other L ranges and considering e5. The correlation matrix contains the satellite coordinates: L, Latitude, as well as cos(MLT) and sin(MLT). These last two variables are used instead of MLT alone to avoid discontinuities when passing from MLT = 23H to MLT = 0H. As already mentioned, only two solar wind parameters (speed and flow pressure) and two geomagnetic indexes were selected. The correlation is more significant between the fluxes and the solar wind speed (31%) and the SYM/H index (35%), weaker with the flow pressure, sin(MLT), the AL index and the latitude (10%, 13%, 14%, and 21%, respectively) and even less important with the other variables. The solar wind and the geomagnetic parameters are strongly correlated, what provokes a decrease of the correlation when both groups of parameters are considered together as inputs for the training procedure as shown later.

Finally, eight groups of input variables were selected to perform correlation tests that allowed to choose the best one for the model training:
Group 0: Log(fluxes)
Group 1: Log(fluxes), SYM/H
Group 2: Log(fluxes), SYM/H, AL
Group 3: Log(fluxes), L, cos(MLT), sin(MLT), Latitude
Group 4: Log(fluxes), SYM/H, L, cos(MLT), sin(MLT), Latitude
Group 5: Log(fluxes), L, cos(MLT), sin(MLT), Latitude, SWSpeed, SWPressure
Group 6: Log(fluxes), SYM/H, L, cos(MLT), sin(MLT), Latitude, SWSpeed, SWPressure
Group 7: Log(fluxes), SYM/H, Latitude, SWSpeed

4. Results and Discussion

The usual Root Mean Square Error (RMSE) and the Spearman Correlation Coefficient (r) were employed to compare the predicted Log(e) values (obtained with the developed LSTM model using the train data set series) with the corresponding observation subseries of the out-of-sample test data set. The Prediction Efficiency (PE) has also been evaluated to assess the forecasts as follows:

$$\text{PE} = 1 - \frac{\sum (Y_i - X_i)^2}{\sum (X_i - \hat{X})^2} \tag{9}$$

Table 1
Correlation Metrics (RMSE and r Parameters) for the Input Groups 0–7 Evaluated With LSTM Model for the Hourly Time Series at L = X − 8 R$_E$ With X = 1,2,3 Using Log(e1)

	RMSE	r	RMSE	r	RMSE	r
Group	L = 1–8 R$_E$		L = 2–8 R$_E$		L = 3–8 R$_E$	
0_baseline	0.801	0.221	0.711	0.419	0.354	0.844
0	0.391	0.794	0.388	0.810	0.232	0.931
1	0.385	0.802	0.382	0.816	0.225	0.935
2	0.393	0.796	0.392	0.804	0.227	0.934
3	0.331	0.858	0.342	0.856	0.212	0.943
4	*0.324*	*0.864*	0.345	0.855	*0.204*	*0.947*
5	0.331	0.858	0.347	0.851	0.214	0.942
6	0.334	0.864	*0.324*	*0.864*	0.206	0.946
7	0.342	0.849	0.341	0.858	0.210	0.944

Note. The 0_baseline reports the metrics evaluated with the persistence model. The bold-italic values represent the best results for each *L* region.

where Y_i, X_i, and $\hat{X}$ are the predictions, observations, and the observations average, respectively. In addition, novel metrics based on the log accuracy ratio $R = \log(Y_i/X_i)$ introduced by Morley et al. (2018) are applied to the results (Y_i, X_i represent here the untransformed fluxes). These metrics are the Median Symmetric Accuracy:

$$\text{MSA} = 100 \left(\exp(\text{Median}(|\log(R)|)) - 1 \right) \qquad (10)$$

and the Symmetric Signed Percentage Bias:

$$\text{SSPB} = 100 \, \text{sgn} \left(\text{Median}(\log(R)) \right) (\exp(|\text{Median}(\log(R))|) - 1) \qquad (11)$$

These metrics present the advantages of being robust to efficiently deal with data distributed over several orders of magnitude and presenting outliers. They are easily interpretable and directly provide the evaluation of the untransformed fluxes, which are the focused physical quantities by the users. The Space Weather community suggests their use to validate the performance of the radiation belts environment models with the object of screening their operational applicability in the evaluation of Space Weather effects (Zheng et al., 2019).

Results are presented in the next subsections by evaluating the metrics that compare the predictions with the corresponding out-of-sample test set. Log(e1) fluxes are employed to discuss the analysis of different input groups, *L* ranges, time step units and time step look-back since similar trends are obtained with Log(e5), for which the results are only shown for the best metrics case and particular differences from Log(e1) fluxes. The predictions involve only one time step in the future, that is, 1 hr for 1-hr resolution and 1 day for 1-day resolution. Finally, some preliminary results of multi-step prediction are also discussed.

4.1. Comparing Input Features

The eight input groups selected in the previous section present, in general, very similar good metrics of RMSE and *r* values, as noticed from Table 1 for Log(e1) considering the different *L* ranges, where we can roughly assume that only the outer belt is included for L = 3–8 R$_E$, the slot region is added for of L = 2–8 R$_E$ and finally the inner belt is also incorporated for L = 1–8 R$_E$. The 0_baseline row reports metrics for a baseline ML persistence model where the observation of the previous time step is used to predict the observation at the next time step. This model is the simplest forecast that can be performed, representing a benchmark for the results of the LSTM model. The baseline results for the outer belt region are accurate enough, but including the other regions drastically impairs the performance. Considering now the LSTM results, some small differences between groups can be highlighted for any *L* range. Groups 1 and 2, adding only geomagnetic indexes series to the corresponding fluxes, provide overall slightly worse correlation and higher total errors. The consideration of AL in group 2 does not seem to provide added value to the inputs. On the contrary, there is an improvement in group 3 by considering only the satellite coordinates. Certainly, the best correlation is obtained with the inclusion of both the satellite coordinates and the SYM/H index (group 4). The addition of the solar wind parameters to the 3rd group (4th group) to define group 5 (group 6) does not exhibit a better correlation, except for the range L = 2–8 R$_E$ (that presents very similar metrics to the range L = 1–8 R$_E$). This is a consequence of the close dependence between solar wind and geomagnetic parameters (as pointed out before), which are already well represented by SYM/H in group 1. Moreover, any subtle nonlinear correlation between the solar wind features and the flux variations could be hidden in the statistical procedure. Furthermore, it is observed that removing the SYM/H parameter in group 5 worsens the metrics compared with group 6. The introduction of solar wind parameters worsens the whole data set of inputs because they contain many gaps contrary to the geomagnetic indexes that do not have any gaps. To overcome such loss of information that constrains dropping all the other data at the times of solar wind data gaps, we have filled the missing data with interpolated values of solar wind parameters. It should be taken in mind that the interpolation remains a fictitious way of retaining more data in the time series and somehow misleading real trends in the training procedure.
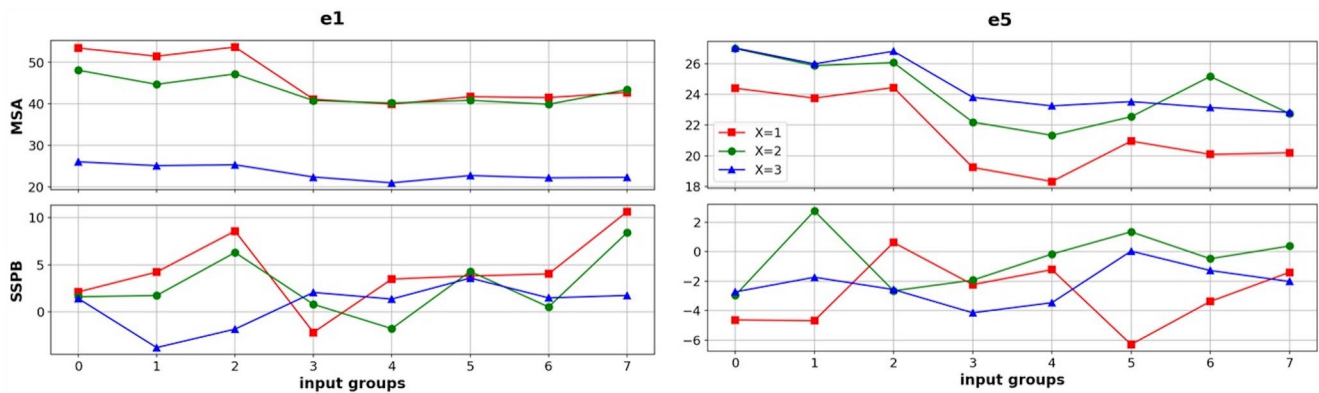
Figure 6. MSA and SSPB metrics (in %) for e1 and e5 and input groups 0–7 evaluated with Long-Short Term Memory model for the hourly time series at $L = X - 8$ R_E with $X = 1, 2, 3$ (red, green, blue). The corresponding values for the baseline model are for e1: MSA = (183.3, 107.6, 58.4), SSPB = (−0.7, 0.4, 0.5) and for e5: MSA = (83.8, 69.9, 67.4), SSPB = (0.9, 1.2, 1.2) in the $X = (1, 2, 3)$ order.

Assessment using MSA and SSPB metrics is displayed in Figure 6 for e1 and e5 EPT channels. MSA confirms for e1 the worst performance of the model when including the slot and the inner belt regions. The opposite behavior is observed for e5 even if the errors keep closer than for e1. Such differences could be partially explained by the fact that the slot and the inner belt regions are more attained by lower energy fluxes generating more variability and, thus, less accuracy in the forecasts. Bias, limited to about |10|%, are very variable when considering the different groups, but from a quick visualization, the e1 (e5) metrics in general demonstrate an overestimation (underestimation) of observations.

Figure 7 displays a good correlation, $r = 0.935, 0.947, 0.946$ between predictions and observations of hourly Log(e1) for input groups 1, 4, 6 where only the outer radiation belt is considered ($L = 3$–8 R_E) with a look-back of 48 hr. The color scale reflects the counts distribution along the flux units. Many points are located very close to the main diagonal and between 10^3 and $10^{5.5}$ electron flux units (EFU). When comparing different L-shell ranges for the input group 4 (yielding the largest correlation) as in Figure 8, we obtain a worse correlation for extended L ranges to the slot region ($L = 2$–8 R_E) and to the inner belt ($L = 1$–8 R_E) represented in the middle and left panel, respectively. Nevertheless, the entire range $L = 1$–8 R_E performs better than considering only the slot region. Deviations from the main diagonal concentrate around the strongest distribution $10^{3.5}$–10^5 EFU whereas for the $L = 2$–8 R_E, the extreme lowest count tail seems to deviate more, showing the limitations of the model to simulate the dropouts and the higher flux increments.

Another aspect to check is the impact of longer look-back periods on the model performance, as displayed in Figure 9. The three panels show 72, 96, and 120 hr of look-back for input group 4 at the outer belt ranges. The
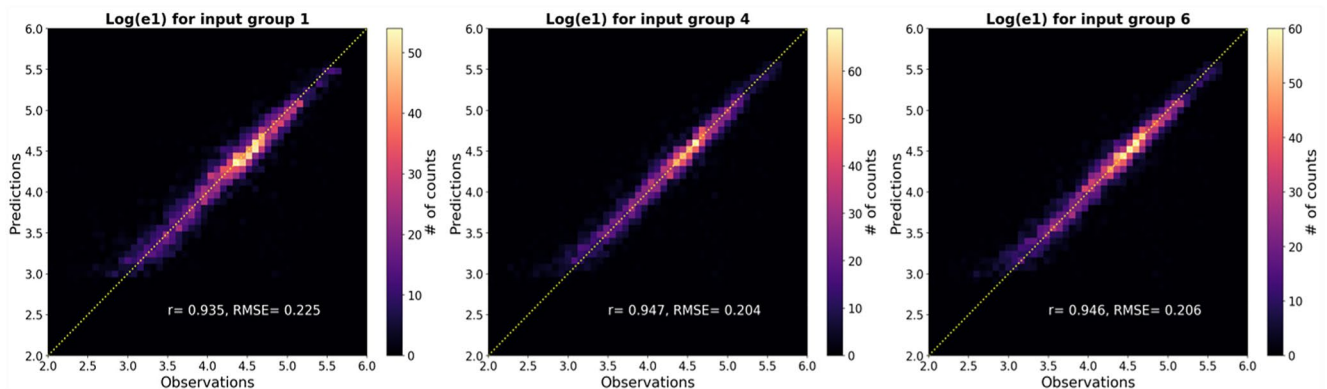

Figure 7. Correlation between hourly Log(e1) observed and predicted fluxes in #/(cm² s sr MeV). From left to right: for groups 1, 4, and 6 for a look-back of 48 hr at $L = 3$–8 R_E.
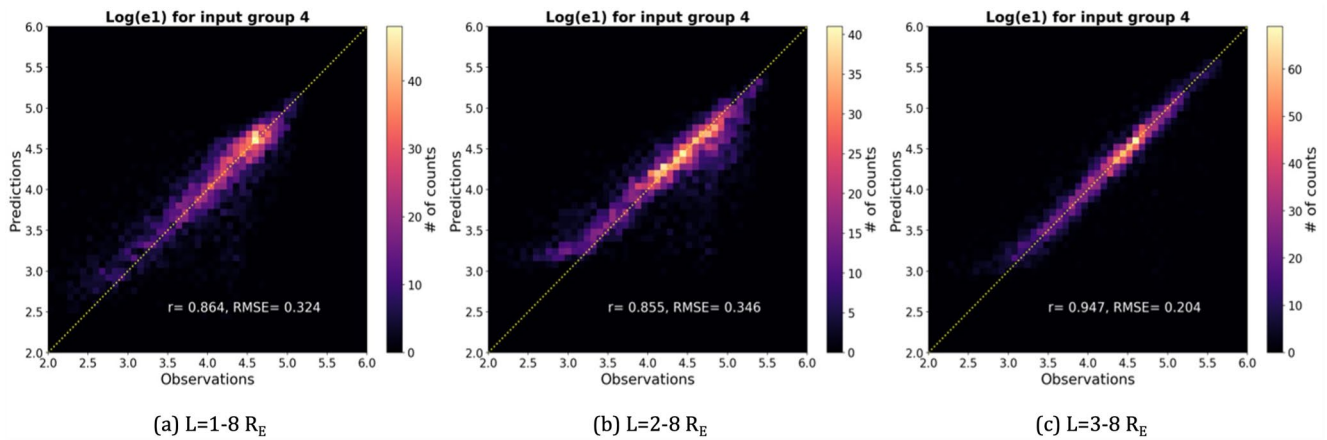
Figure 8. Correlation between hourly Log(e1) observed and predicted fluxes in #/(cm^2 s sr MeV) for input group 4 and for a look-back of 48 hr at different L ranges.

metrics are very similar to the 48 hr look-back meaning that 2 days in the past is enough to obtain a correlation of nearly 0.95 for 1 hr of prediction data.

4.2. Daily and Hourly Time Step Resolution

The time step resolution used in the training scheme is governed by a balance between the model convergence capabilities and the degree of detail desired for the predictions. In Figure 10, a comparison of the same test data set displays, on the left, the daily predictions vs. the hourly predictions on the right. The hourly average allows capturing local variations that are smoothed by the daily average, while worsening the correlation as the resolution is higher. This was also confirmed with 10-min resolution computations, not shown in this paper, that hardly converge to poorer metrics. Both the hourly and the daily model capture the main features of the time series evolution. However, the huge dropouts observed are not well reproduced by the model and should be more deeply investigated in further studies.

4.3. Comparison of Log(e1) and Log(e5) Predictions

Keeping the same NN parameter settings as before, the model obtained for the Log(e5) predictions follows the same trends as Log(e1), with the input group 4 also giving the best metrics. The corresponding logarithmic fluxes, lower than those of e1 as expected, span from around $10^{0.5}$ to 10^3 EFU with small deviations from the main diagonal. However, when broadening the L range to the slot region ($L = 2$–8 R$_E$) and to the inner belt ($L = 1$–8 R$_E$) as in Figure 11, the metrics are still very good. Contrary to the Log(e1) results, the Log(e5) predictions provide better
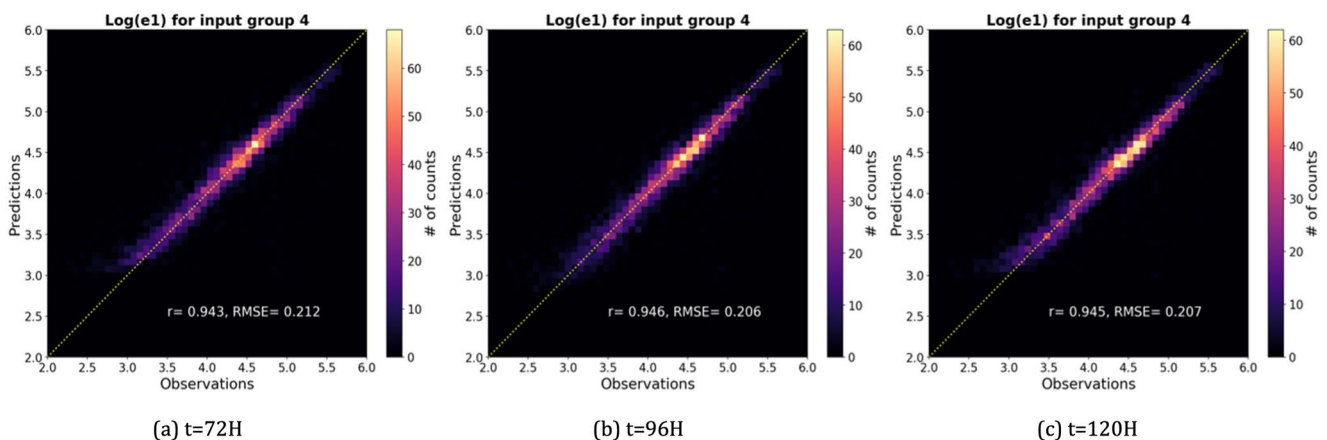

Figure 9. Correlation between hourly Log(e1) observed and predicted fluxes in #/(cm^2 s sr MeV) for group 4 and for a look-back of 72, 96, and 120 hr at $L = 3$–8 R$_E$.
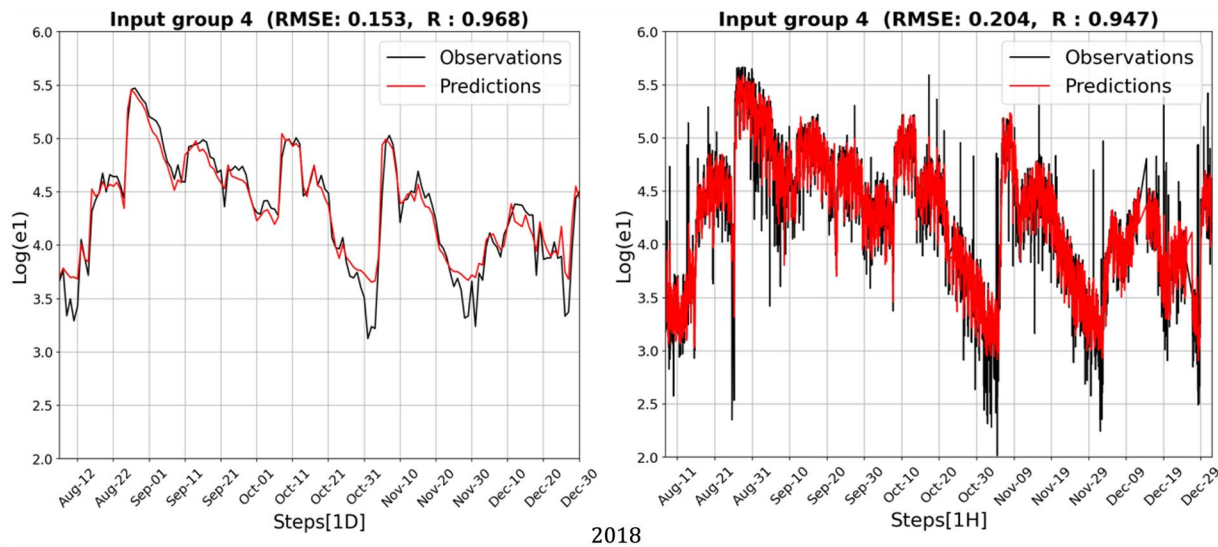
Figure 10. Daily and hourly Log(e1) fluxes in #/(cm^2 s sr MeV) for input group 4 with a look-back of 2 days (left) and 48 hr (right) at $L = 3$–8 R$_E$.

correlation and lower total errors for the whole L range. It is also interesting to note that the huge dropouts are better captured for Log(e5) as noticed when comparing plots from the left with those from the right in Figure 12 for two ranges of L-shell: (a) inner belt included and (b) only outer belt. This explains, to some extent, the better metrics obtained for the higher energy channel predictions of Log(e5).

4.4. Prediction of Several Steps Ahead

The same model design has been trained to forecast the Log(e1) and Log(e5) fluxes for a sequence of steps ahead in a unique execution. In Table 2, the metrics of a simulation considering 48 hr look-back and 12 hr ahead are reported for each hour of the simultaneous forecast. The performance is slightly poorer than for one-step forecasts, but it is still very good, in particular for the first steps, and very promising for further investigations. Here, the RMSE (MSA) errors remain smaller (higher) for the fluxes of higher energy than for those of lower energy. Different from the case of one-step simulations, correlation coefficients are worse for higher energy fluxes. The Bias reveals a small nearly systematic underestimation. Figure 13 displays an example of a look-back + forecast period of 48 + 12 hr chosen for September 2018, as an illustration, among those contained in the sample test series. It is important to mention that a more systematic analysis should help to infer the most reliable multistep sequence for a desired threshold metrics.
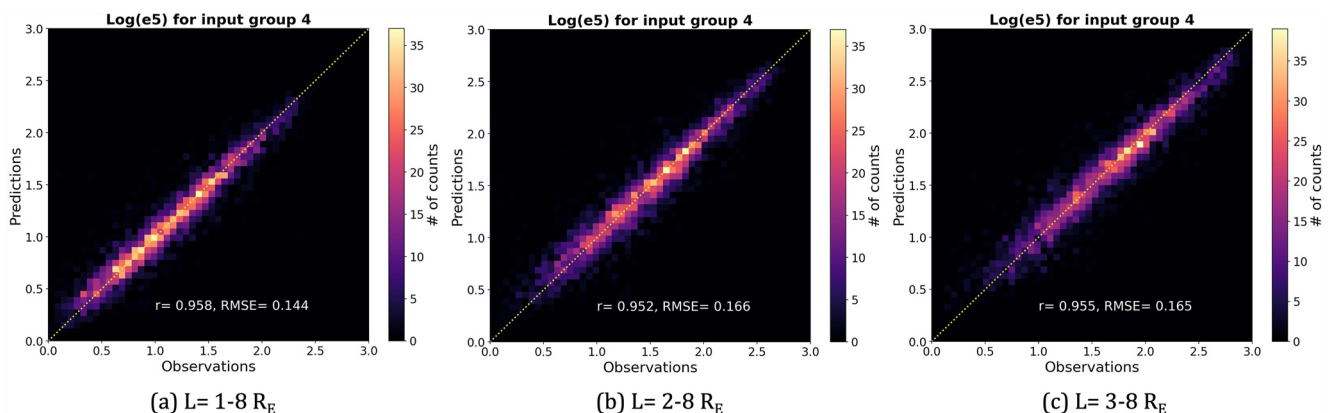

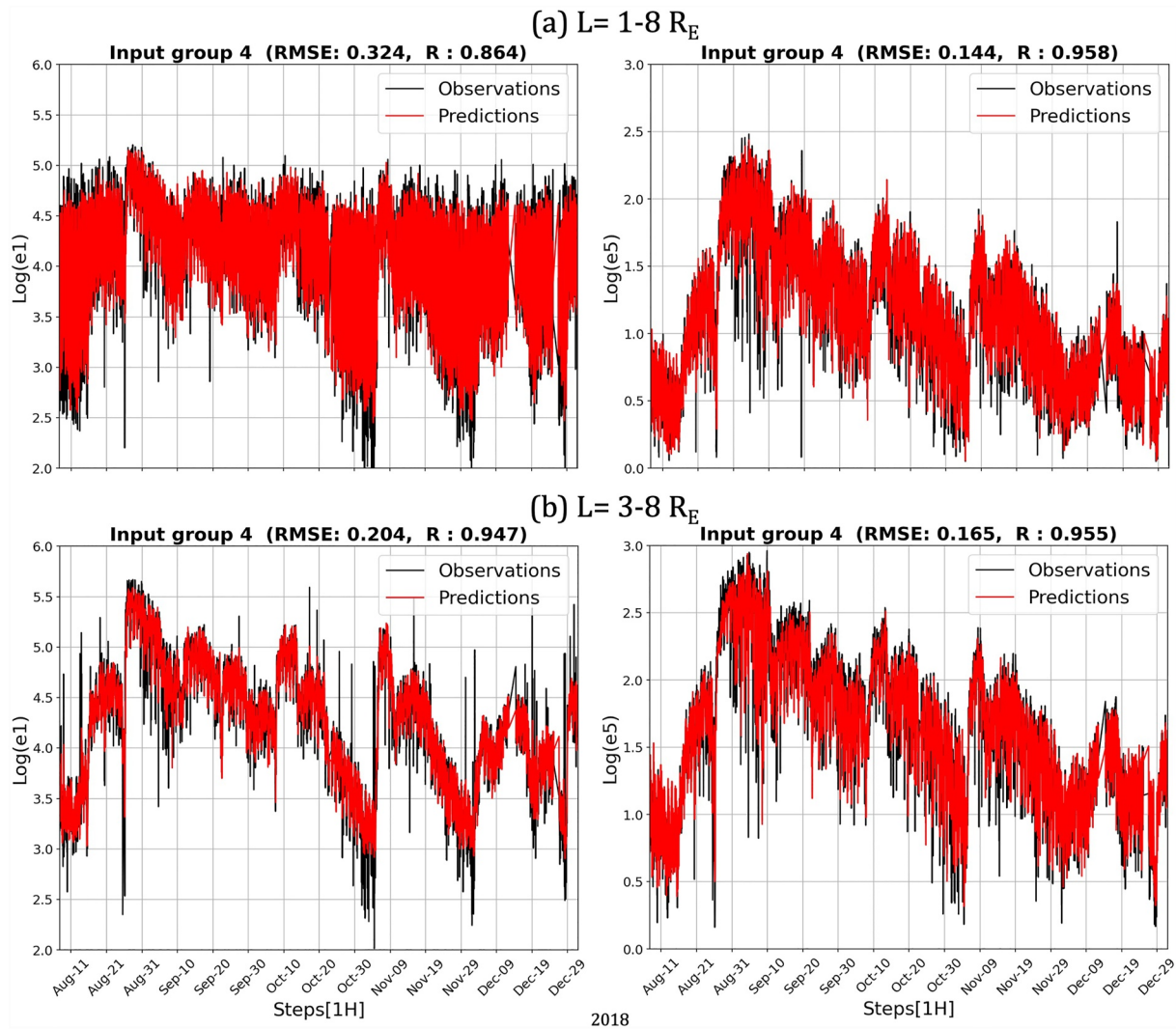**Figure 11.** Same as Figure 8, but for Log(e5) fluxes.

Figure 12. Hourly fluxes in #/(cm^2 s sr MeV) for input group 4 with a look-back of 48 hr for Log(e1) on the left and Log(e5) on the right at (a) $L = 1$–8 R$_E$ (top plots) and (b) $L = 3$–8 R$_E$ (bottom plots).

5. Conclusions

For the first time, the PROBA-V/EPT electron fluxes have been used to train a Neural Networks model for radiation belt forecasting. The LSTM method has been selected as deep learning Neural Network to better consider the long-term and short-term dependences of the time series variables. The satellite coordinates as well as external Geomagnetic indexes and Solar Wind data have also been joined to the series of input variables, employed to assess the performance of the model guided by different groups of parameters. It has been found that merging the electron fluxes with the satellite coordinates and the SYM/H geomagnetic indexes results roughly in the best metrics for both the non-relativistic 500–600 keV and the relativistic 1.0–2.4 MeV energy channels. The addition of Solar Wind parameters does not lead to an improvement in the model configuration for these simulations. On the contrary, their effects seem to be overlapped with the influence provided by the SYM-H geomagnetic index. A preparatory interpolation made out to keep as much data as possible could also influence the real trends of Solar Wind parameters. The 1-hr resolution model provides a reasonable equilibrium between a detailed dynamics description and the model performance. Looking back 2 days in the past appears enough to predict the next step, either for the hourly or the daily resolution. Unfortunately, the total reconstruction of the L-time 3D space is less feasible at such resolutions since PROBA-V crosses very quickly (in about 10 min and near the poles) all the L-shells along its orbit period. The inclusion of the slot region and the inner belt worsens the metrics for the

Table 2
Metrics for Log(e1) and Log(e5) Predictions Using Group 4 Inputs With the Hourly Time Series at L = 3–8 R_E Considering 48 hr Look-Back and 12 hr Ahead

Hs ahead	Log(e1)			e1		Log(e5)			e5	
	RMSE	r	PE	MSA	SSPB	RMSE	r	PE	MSA	SSPB
1	0.241	0.926	0.856	32.7	−3.1	0.223	0.917	0.840	34.8	−3.6
2	0.260	0.915	0.833	34.2	−2.0	0.235	0.907	0.823	38.1	−4.3
3	0.256	0.917	0.838	35.0	−3.0	0.238	0.905	0.818	37.1	−0.8
4	0.277	0.904	0.810	37.8	−0.8	0.237	0.906	0.820	37.0	−2.5
5	0.264	0.911	0.827	37.0	−1.8	0.247	0.898	0.805	39.1	−1.3
6	0.275	0.902	0.812	40.7	−5.7	0.252	0.892	0.796	41.3	−4.6
7	0.287	0.893	0.796	41.6	−3.6	0.265	0.881	0.774	44.3	−0.8
8	0.286	0.893	0.797	42.8	−6.9	0.270	0.876	0.767	44.1	−3.7
9	0.300	0.883	0.776	43.4	−3.3	0.273	0.874	0.761	44.7	−0.1
10	0.289	0.890	0.792	41.2	−4.7	0.277	0.870	0.754	45.0	0.0
11	0.297	0.885	0.781	43.1	−1.0	0.281	0.866	0.746	46.2	1.1
12	0.299	0.882	0.778	43.4	−1.4	0.281	0.866	0.747	45.3	−0.3

Note. Corresponding metrics for e1 and e5.

lower energy predictions from about $r{\sim}0.95$ (RMSE ∼ 0.20) to $r \sim 0.85$ (RMSE ∼ 0.35), whereas the metrics remain well correlated at $r \sim 0.95$ and with very low total errors (RMSE ∼ 0.16) when extending the L range for the higher energies. The lower RMSE errors for the high energies come from a better capture of the huge dropouts and their significant MSA lower errors when adding the lower L regions to the forecast could be related to less flux variability in time than for low energy fluxes. Simulations considering simultaneously a sequence of steps ahead, even worsening the metrics, demonstrate still reliable capabilities of the fitted model and its potential implementation in operational frameworks. In general, the bias remained relatively small at no more than 10%.

Further work is still needed to completely tune the present model to predict the electron flux of the radiation belts at LEO with high accuracy. A reprocessing of the data, as in the SHELLS model (Boyd et al., 2023), could be considered to remove orbital effects on flux variations at different longitudes, and thus, to enable the use of high resolutions down to 1 min. More data over the next years will contribute to completing an entire solar cycle
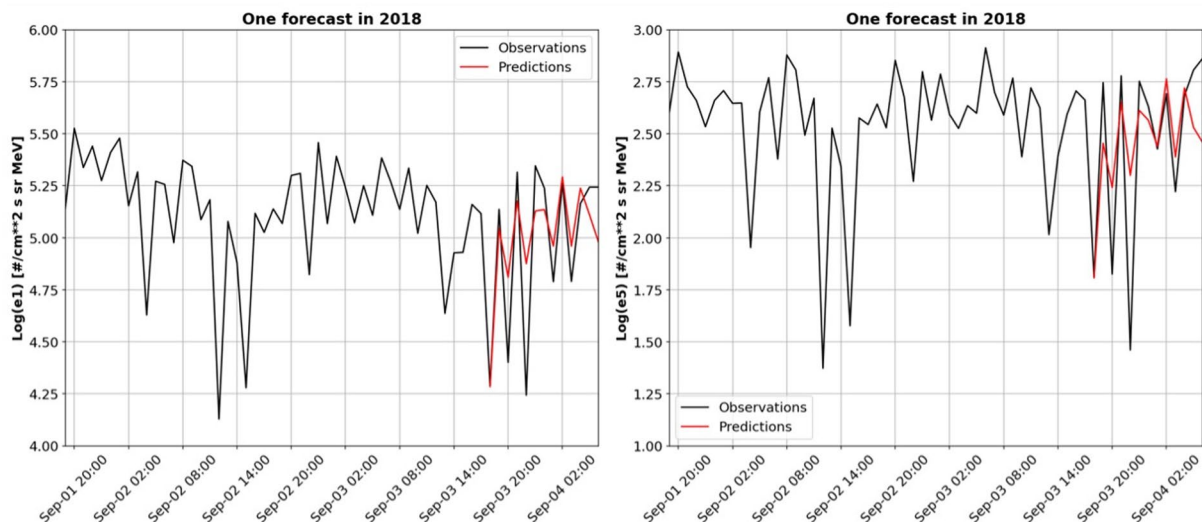

Figure 13. One forecast of 12 hr in red over the sample test series for 48 hr of look-back considering input group 4 to predict: (left) Log(e1) and (right) Log(e5) fluxes at $L = 3–8$ R_E.

of flux measurements that will refine the training of the model. New multidirectional measurements from the 3-Dimensional Energetic Electron Spectrometer (3DEES) instrument that will be launched onboard PROBA-3 in 2024 will extend the resources to improve the model together with the addition of other multi-satellite data. Supplementary efforts should also be invested to introduce more physics knowledge to produce robust learning mechanisms capable of converging faster toward optimal solutions. For example, customizing the loss functions by introducing specific equations of the radiation belt dynamics could accelerate such achievements.

Data Availability Statement

The electron fluxes are publicly available at https://swe.ssa.esa.int/space-radiation upon registration on the ESA SSA website. The Solar Wind parameters and geomagnetic indices are publicly available at https://omniweb.gsfc.nasa.gov/. The processed text csv data files used as input and the corresponding Python 3.9 code elaborated to generate the Machine Learning model and data results for the study are available at (Botek et al., 2023) with Creative Commons Attribution 4.0 International licence.

References

Abadi, M., Agarwal, A., Barham, P., Brevdo, E., Chen, Z., Citro, C., et al. (2016). TensorFlow: Large-scale machine learning on heterogeneous distributed systems [Software]. ArXiv Preprint ArXiv:1603.04467. http://arxiv.org/abs/1603.04467

Baker, D. N. (2021). Wave–particle interaction effects in the Van Allen belts. *Earth Planets and Space*, *73*(1), 189. https://doi.org/10.1186/s40623-021-01508-y

Botek, E., Pierrard, V., & Winant, A. (2023). Prediction of radiation belts electron fluxes at a Low earth Orbit using neural networks with PROBA-V/EPT data (version V1). [Dataset] and [Software]. Zenodo. https://doi.org/10.5281/zenodo.7801368

Boyd, A. J., Green, J. C., O'Brien, T. P., & Claudepierre, S. G. (2023). Specifying high altitude electrons using low-altitude LEO systems: Updates to the SHELLS model. *Space Weather*, *21*(3), e2022SW003338. https://doi.org/10.1029/2022sw003338

Chu, X., Ma, D., Bortnik, J., Tobiska, W. K., Cruz, A., Bouwer, S. D., et al. (2021). Relativistic electron model in the outer radiation belt using a neural network approach. *Space Weather*, *19*(12), e2021SW002808. https://doi.org/10.1029/2021sw002808

Claudepierre, S. G., & O'Brien, T. P. (2020). Specifying high-altitude electrons using low-altitude LEO systems: The shells model. *Space Weather*, *18*(3), e2019SW002402. https://doi.org/10.1029/2019sw002402

Cunningham, G. S., Botek, E., Pierrard, V., Cully, C., & Ripoll, J. F. (2020). Observation of high-energy electrons precipitated by NWC transmitter from PROBA-V low-Earth orbit satellite. *Geophysical Research Letters*, *47*(16), e2020GL089077. https://doi.org/10.1029/2020GL089077

Cyamukungu, M., Benck, S., Borisov, S., Gregoire, G., Cabrera, J., Bonnet, J. L., et al. (2014). The energetic particle telescope (EPT) on board PROBA-V: Description of a new science-class instrument for particle detection in space. *IEEE Transactions on Nuclear Science*, *61*(6), 3667–3681. https://doi.org/10.1109/TNS.2014.2361955

de Lima, R., Chen, Y., & Lin, Y. (2020). Forecasting megaelectron-volt electrons inside Earth's outer radiation belt: PreMevE 2.0 based on supervised machine learning algorithms. *Space Weather*, *18*(2), e2019SW002399. https://doi.org/10.1029/2019SW002399

Garrett, H. B. (2016). *Spacecraft charging*. CRC Press.

Géron, A. (2022). *Hands-on machine learning with Scikit-Learn, Keras, and TensorFlow*. O'Reilly Media, Inc.

Hochreiter, S., & Schmidhuber, J. (1997). Long short-term memory. *Neural Computation*, *9*(8), 1735–1780. https://doi.org/10.1162/neco.1997.9.8.1735

Koskinen, H. E. J., & Kilpua, E. K. J. (2022). *Physics of Earth's radiation belts: Theory and observations*. Springer Nature.

Landis, D. A., Saikin, A. A., Zhelavskaya, I., Drozdov, A. Y., Aseev, N., Shprits, Y. Y., et al. (2022). NARX neural network derivations of the outer boundary radiation belt electron flux. *Space Weather*, *20*(5), e2021SW002774. https://doi.org/10.1029/2021SW002774

Li, W., & Hudson, M. K. (2019). Earth's Van Allen radiation belts: From discovery to the Van Allen Probes era. *Journal of Geophysical Research: Space Physics*, *124*(11), 8319–8351. https://doi.org/10.1029/2018ja025940

Ma, D., Bortnik, J., Chu, X., Claudepierre, S. G., Kellerman, A., & Ma, Q. (2022). Opening the black box of the radiation belt machine learning model. ArXiv Preprint ArXiv:2208.08905 Retrieved from http://arxiv.org/abs/2208.08905

Ma, D., Chu, X., Bortnik, J., Claudepierre, S. G., Tobiska, W. K., Cruz, A., et al. (2022). Modeling the dynamic variability of sub-relativistic outer radiation belt electron fluxes using machine learning. *Space Weather*, *20*(8), e2022SW003079. https://doi.org/10.1029/2022SW003079

Mann, I. R., Ozeke, L. G., Murphy, K. R., Claudepierre, S. G., Turner, D. L., Baker, D. N., et al. (2016). Explaining the dynamics of the ultra-relativistic third Van Allen radiation belt. *Nature Physics*, *12*(10), 978–983. https://doi.org/10.1038/nphys3799

Mauk, B. H., Fox, N. J., Kanekal, S. G., Kessel, R. L., Sibeck, D. G., & Ukhorskiy, A. Y. (2012). Science objectives and rationale for the radiation belt storm probes mission. In *The Van Allen probes mission* (pp. 3–27). Springer.

McIlwain, C. E. (1961). Coordinates for mapping the distribution of magnetically trapped particles. *Journal of Geophysical Research*, *66*(11), 3681–3691. https://doi.org/10.1029/jz066i011p03681

Morley, S. K., Brito, T. V., & Welling, D. T. (2018). Measures of model performance based on the log accuracy ratio. *Space Weather*, *16*(1), 69–88. https://doi.org/10.1002/2017sw001669

Myagkova, I., Efitorov, A., Shiroky, V., & Dolenko, S. (2019). Quality of prediction of daily relativistic electrons flux at geostationary orbit by machine learning methods. In *International conference on artificial neural networks* (pp. 556–565).

Pierrard, V., Botek, E., Ripoll, J. F., & Cunningham, G. (2020). Electron dropout events and flux enhancements associated with geomagnetic storms observed by PROBA-V/energetic particle telescope from 2013 to 2019. *Journal of Geophysical Research: Space Physics*, *125*(12), e2020JA028487. https://doi.org/10.1029/2020JA028487

Pierrard, V., Lopez Rosson, G., Borremans, K., Lemaire, J., Maes, J., Bonnewijn, S., et al. (2014). The energetic particle telescope: First results. *Space Science Reviews*, *184*(1–4), 87–106. https://doi.org/10.1007/s11214-014-0097-8

Pierrard, V., Lopez-Rosson, G., & Botek, E. (2019). Dynamics of megaelectron volt electrons observed in the inner belt by PROBA-V/EPT. *Journal of Geophysical Research: Space Physics*, *124*(3), 1651–1659. https://doi.org/10.1029/2018JA026289

Pierrard, V., Ripoll, J.-F., Cunningham, G., Botek, E., Santolik, O., Thaller, S., et al. (2021). Observations and simulations of dropout events and flux decays in October 2013: Comparing MEO equatorial with LEO polar orbit. *Journal of Geophysical Research: Space Physics*, *126*(6), e2020JA028850. https://doi.org/10.1029/2020ja028850

Pierrard, V., Winant, A., Botek, E., Ripoll, J.-F., Cosmides, M., & Malaspina, D. M., et al. (2022). Simultaneous observations of the 23 June 2015 intense storm at at low Earth orbit and geostationary transfer orbit. *URSI Radio Science Letters*, *4*. https://doi.org/10.46620/22-0016

Reeves, G. D., Friedel, R. H. W., Larsen, B. A., Skoug, R. M., Funsten, H. O., Claudepierre, S. G., et al. (2016). Energy-dependent dynamics of keV to MeV electrons in the inner zone, outer zone, and slot regions. *Journal of Geophysical Research: Space Physics*, *121*(1), 397–412. https://doi.org/10.1002/2015ja021569

Reeves, G. D., McAdams, K. L., Friedel, R. H. W., & O'brien, T. P. (2003). Acceleration and loss of relativistic electrons during geomagnetic storms. *Geophysical Research Letters*, *30*(10), 1529. https://doi.org/10.1029/2002gl016513

Smirnov, A. G., Berrendorf, M., Shprits, Y. Y., Kronberg, E. A., Allison, H. J., Aseev, N. A., et al. (2020). Medium energy electron flux in Earth's outer radiation belt (MERLIN): A machine learning model. *Space Weather*, *18*(11), e2020SW002532. https://doi.org/10.1029/2020SW002532

Son, J., Moon, Y.-J., & Shin, S. (2022). 72-hour time series forecasting of hourly relativistic electron fluxes at geostationary orbit by deep learning. *Space Weather*, *20*(10), e2022SW003153. https://doi.org/10.1029/2022sw003153

Sun, X., Lin, R., Liu, S., He, X., Shi, L., Luo, B., et al. (2021). Modeling the relationship of ≥2 MeV electron fluxes at different longitudes in geostationary orbit by the machine learning method. *Remote Sensing*, *13*(17), 3347. https://doi.org/10.3390/rs13173347

Thorne, R. M., Li, W., Ni, B., Ma, Q., Bortnik, J., Chen, L., et al. (2013). Rapid local acceleration of relativistic radiation-belt electrons by magnetospheric chorus. *Nature*, *504*(7480), 411–414. https://doi.org/10.1038/nature12889

Turner, D. L., Kilpua, E. K. J., Hietala, H., Claudepierre, S. G., O'Brien, T. P., Fennell, J. F., et al. (2019). The response of Earth's electron radiation belts to geomagnetic storms: Statistics from the Van Allen Probes era including effects from different storm drivers. *Journal of Geophysical Research: Space Physics*, *124*(2), 1013–1034. https://doi.org/10.1029/2018JA026066

Wanliss, J. A., & Showalter, K. M. (2006). High-resolution global storm index: Dst versus SYM-H. *Journal of Geophysical Research*, *111*(A2), A02202. https://doi.org/10.1029/2005ja011034

Wei, L., Zhong, Q., Lin, R., Wang, J., Liu, S., & Cao, Y. (2018). Quantitative prediction of high-energy electron integral flux at geostationary orbit based on deep learning. *Space Weather*, *16*(7), 903–916. https://doi.org/10.1029/2018SW001829

Weygand, J. M., Zesta, E., & Troshichev, O. (2014). Auroral electrojet indices in the Northern and Southern Hemispheres: A statistical comparison. *Journal of Geophysical Research: Space Physics*, *119*(6), 4819–4840. https://doi.org/10.1002/2013ja019377

Wing, S., Johnson, J. R., Turner, D. L., Ukhorskiy, A. Y., & Boyd, A. J. (2022). Untangling the solar wind and magnetospheric drivers of the radiation belt electrons. *Journal of Geophysical Research: Space Physics*, *127*(4), e2021JA030246. https://doi.org/10.1029/2021JA030246

Wing, S., Turner, D. L., Ukhorskiy, A. Y., Johnson, J. R., Sotirelis, T., Nikoukar, R., & Romeo, G. (2022). Modeling radiation belt electrons with information theory informed neural networks. *Space Weather*, *20*(8), e2022SW003090. https://doi.org/10.1029/2022SW003090

Zheng, Y., Ganushkina, N. Y., Jiggens, P., Jun, I., Meier, M., Minow, J. I., et al. (2019). Space radiation and plasma effects on satellites and aviation: Quantities and metrics for tracking performance of space weather environment models. *Space Weather*, *17*(10), 1384–1403. https://doi.org/10.1029/2018sw002042